Icarus 206 (2010) 139–151

Contents lists available at ScienceDirect

Icarus

journal homepage: www.elsevier.com/locate/icarus

# A comparison of global models for the solar wind interaction with Mars

D. Brain [a,*], S. Barabash [b], A. Boesswetter [c], S. Bougher [d], S. Brecht [e], G. Chanteur [f], D. Hurley [g], E. Dubinin [h], X. Fang [i], M. Fraenz [h], J. Halekas [a], E. Harnett [j], M. Holmstrom [b], E. Kallio [k], H. Lammer [l], S. Ledvina [a], M. Liemohn [d], K. Liu [k], J. Luhmann [a], Y. Ma [m], R. Modolo [n,o], A. Nagy [d], U. Motschmann [c], H. Nilsson [b], H. Shinagawa [p,q], S. Simon [r], N. Terada [p,q]

[a] University of California, UC Berkeley Space Sciences Lab, 7 Gauss Way, Berkeley, CA 94720, USA
[b] Swedish Institute of Space Physics, Kiruna, Sweden
[c] Institute for Theoretical Physics, TU Braunschweig, Germany
[d] Atmospheric, Oceanic, and Space Sciences Department, University of Michigan, Ann Arbor, MI, USA
[e] Bay Area Research Corporation, Orinda, CA, USA
[f] CETP-IPSL, 10–12 avenue de l'Europe, 78140, Vélizy, France
[g] Applied Physics Laboratory, Johns Hopkins University, Laurel, MD, USA
[h] Max-Planck-Institut für Aeronomie, Katlenburg-Lindau, Germany
[i] Laboratory for Atmospheric and Space Physics, University of Colorado at Boulder, Boulder, CO, USA
[j] Department of Earth and Space Sciences, University of Washington, Seattle, WA, USA
[k] Finnish Meteorological Institute, Helsinki, Finland
[l] Space Research Institute, Austrian Academy of Sciences, Austria
[m] Institute for Geophysics and Planetary Physics, University of California, Los Angeles, CA, USA
[n] Swedish Institute of Space Physics, Uppsala, Sweden
[o] LAMTOS/IPSL/UVSQ, 10–12 avenue de l'Europe, 78140, Vélizy, France
[p] National Institute of Information and Communications Technology, Tokyo, Japan
[q] CREST, Japan Science and Technology Agency, Saitama, Japan
[r] Institute of Geophysics and Meteorology, University of Cologne, Cologne, Germany

ARTICLE INFO

*Article history:*
Received 9 October 2008
Revised 21 May 2009
Accepted 28 June 2009
Available online 7 July 2009

*Keywords:*
Mars
Solar wind
Ionospheres
Atmospheres, Evolution

ABSTRACT

We present initial results from the first community-wide effort to compare global plasma interaction model results for Mars. Seven modeling groups participated in this activity, using MHD, multi-fluid, and hybrid assumptions in their simulations. Moderate solar wind and solar EUV conditions were chosen, and the conditions were implemented in the models and run to steady state. Model output was compared in three ways to determine how pressure was partitioned and conserved in each model, the location and asymmetry of plasma boundaries and pathways for planetary ion escape, and the total escape flux of planetary oxygen ions. The two participating MHD models provided similar results, while the five sets of multi-fluid and hybrid results were different in many ways. All hybrid results, however, showed two main channels for oxygen ion escape (a pickup ion 'plume' in the hemisphere toward which the solar wind convection electric field is directed, and a channel in the opposite hemisphere of the central magnetotail), while the MHD models showed one (a roughly symmetric channel in the central magnetotail). Most models showed a transition from an upstream region dominated by plasma dynamic pressure to a magnetosheath region dominated by thermal pressure to a low altitude region dominated by magnetic pressure. However, calculated escape rates for a single ion species varied by roughly an order of magnitude for similar input conditions, suggesting that the uncertainties in both the current and integrated escape over martian history as determined by models are large. These uncertainties are in addition to those associated with the evolution of the Sun, the martian dynamo, and the early atmosphere, highlighting the challenges we face in constructing Mars' past using models.



## 1. Introduction

Mars provides a complex obstacle to the solar wind that varies on all timescales. Incident solar wind at Mars encounters an extended hot exosphere, a conductive ionosphere, and strong localized crustal magnetic fields. Therefore, the martian interaction has elements of the plasma interactions at comets, Venus or Titan, and globally or locally magnetized Solar System objects such as Earth or the Moon. Studies of particles and fields near Mars over the past four decades have not only provided an ever-improving picture of the structure and dynamics of the global plasma

* Corresponding author. Fax: +1 510 643 8302.
*E-mail address:* brain@ssl.berkeley.edu (D. Brain).

0019-1035/$ - see front matter © 2009 Elsevier Inc. All rights reserved.
doi:10.1016/j.icarus.2009.06.030

environment, but have also improved our understanding of processes that can affect atmospheric evolution, the energetics of the upper atmosphere, and Solar System plasma processes.

Computer models of the global plasma environment at Mars have a long heritage. The first simulations of the global martian solar wind interaction were published by Dryer and Heckmann (1967) and Spreiter et al. (1970). Since these initial gasdynamic models, the last 40 years (and especially the last decade) have seen continued advances in the number, variety, and sophistication of global plasma models for Mars. We count at least seven presently active modeling groups using MHD, Hall MHD, multi-fluid, and hybrid approaches (Ma and Nagy, 2007; Terada et al., 2009a; Harnett and Winglee, 2007; Brecht and Ledvina, 2006; Kallio et al., 2006; Boesswetter et al., 2007; Modolo et al., 2006). Combinations of models (e.g. MHD and test particle) are also used to investigate the plasma environment (Cravens et al., 2002; Fang et al., 2008). Additional models may come on line in the near future. Most models are now fully three-dimensional (3D) and follow multiple ion species. In addition to their physical assumptions, the models differ in terms of their implementation and treatment of the simulation boundaries, including the martian crustal magnetic fields.

The presently active global plasma models are used for a variety of purposes at Mars. Nearly all of them have been used to study the rate of ion escape from the atmosphere (e.g. Ma et al., 2002, 2004; Ma and Nagy, 2007; Terada et al., 2009a; Harnett and Winglee, 2006; Brecht and Ledvina, 2006; Kallio et al., 2006; Modolo et al., 2005; Chaufray et al., 2007; Fang et al., in press). Models have also been used to investigate the structure and topology of magnetic fields in the martian system (e.g. Ma et al., 2002; Liemohn et al., 2006, 2007; Harnett and Winglee, 2003; Brecht, 1990, 1997; Brecht and Ferrante, 1991; Brecht et al., 1993; Kallio et al., 2006), the influence of the solar wind on the ionosphere (e.g. Ma et al., 2004; Harnett and Winglee, 2007), plasma boundaries (e.g. Ma et al., 2002, 2004; Harnett and Winglee, 2003; Simon et al., 2007; Boesswetter et al., 2004; Modolo et al., 2006), and charged particle transport near Mars (e.g. Liemohn et al., 2006, 2007; Fang et al., 2008, in press). Dedicated versions of these models have been developed to investigate several physical processes occurring in the martian environment such as energetic neutral atom production and transport (Gunnell et al., 2006, and references therein) or X-ray emission (Gunnell et al., 2005; Koutroumpa et al., 2006). The models are used to simulate the interaction considering conditions that may have existed in the past to trace the evolution of the system over history (e.g. Barabash et al., 2007a; Terada et al., 2009a), and to provide global context for specific spacecraft observations (e.g. Ma et al., 2004; Kallio et al., 2006; Boesswetter et al., 2007, 2009; Modolo et al., 2006). In general, the models are tools that can be used to study the effects of different drivers on the martian system, reveal the physical processes important in the interaction, and place existing observations in both current and historical context.

The proliferation of models provides a variety of means of probing the global martian plasma interaction, but also creates some challenges in interpretation for the larger community. One challenge is knowing which models are appropriate for a given problem. The characteristics of the different models make them best-suited to certain types of investigations, so that no model approach is always superior to the others. The strengths and limitations of the MHD and hybrid approaches are discussed in the literature (cf. Nagy et al., 2004; Ledvina et al., 2008), but the differences between models of the same type are more subtle. Different choices in time step, grid size, boundary conditions, or included processes determine which science questions can be addressed. Another issue occurs when multiple models study the same question and disagree on the answer, leaving uncertainty in the community about which (if any) model is correct. In this situation it is often difficult to determine whether and/or why the different models disagree because different approaches were taken in addressing the question. For example, several models cited above have calculated ion escape rates in the present epoch, but since different limiting physics, input conditions, species, numerical scheme, etc. were used it is not straightforward to determine whether the estimates agree or disagree. In summary, selection of the appropriate model for a task requires familiarity not only with the relevant physics, but also with details of the simulation. As no model is an ideal simulation, those who use them for physical interpretations or insights must be aware of their many assumptions and uncertainties.

An effective way to address some of the issues above is for the community to undertake a model challenge activity where different groups run their models for similar input conditions and compare the results. Model challenge activities are common in other disciplines (magnetic reconnection (Birn et al., 2001); atmospheric circulation and climate modeling (Boer et al., 1991); radiation transfer modeling (Pinty et al., 2001) to name just a few), and provide valuable opportunity to both find errors in the models and probe the physics responsible for differences between the models. Such an activity would provide new or developing models with a set of input conditions and model diagnostics for comparison.

We have formed an international group that is undertaking a model challenge activity for Mars, with involvement from global modeling groups, observers, and experts in the martian upper atmosphere and plasma environment. Our goal is to advance our understanding of the physical processes governing different regions of the martian plasma interaction by intercomparing the different models' results for identical input conditions.

Here we report the results from the first Mars global plasma interaction model comparison for a single set of input conditions. We describe the selected model inputs in Section 2, and the participating models in Section 3. Three different comparisons were performed, and are discussed in Sections 4–6. We focus in this work on intercomparison of model results, rather than comparison to specific observations, and have chosen a variety of quantities for comparison in order to examine the model output across a variety of spatial scales and regions. One-dimensional samples of model pressures are described first in Section 4, and two-dimensional model samples of particle density are described in Section 5. Comparison of the atmospheric escape rates for a single ion species from the different models is given in Section 6, and we follow in Section 7 with a brief summary and discussion of the implications of this work, and future efforts.

## 2. Inputs

A single set of input parameters (Table 1) was chosen to approximate typical solar wind conditions at Mars for solar moderate conditions, and run for all models. The incident solar wind ions are protons with density of 3 $cm^{-3}$ flowing radially from the Sun toward Mars with speed 400 km/s. In the Mars Solar Orbital (MSO)

**Table 1**
Input parameters chosen for the model challenge.

| | |
|---|---|
| Solar wind velocity | 400 km/s |
| Solar wind density | 3 $cm^{-3}$ protons |
| Solar wind proton temperature | 4.3 eV ($5 \times 10^4$ K) |
| Solar wind electron temperature | 25.9 eV ($3 \times 10^5$ K) |
| IMF | 3 nT Parker spiral |
| EUV flux | F10.7 = 130 (solar moderate, Mars equinox) |
| Atmosphere/ionosphere | Supplied by MTGCM |
| Exosphere/corona | None specified |
| Mars | No crustal fields |

coordinate system the incident solar wind flows in the $-x$ direction. The direction opposite the martian orbital velocity vector is in the $+y$ direction, and $+z$ is directed out of the martian orbital plane, completing the right-handed coordinate system. Some models require specified solar wind proton and electron temperatures, in which case values of 4.3 eV and 25.9 eV, respectively, were adopted. The interplanetary magnetic field (IMF) carried by the solar wind is 3 nT, oriented in a Parker spiral (57° from the $-x$ direction, toward $+y$).

Each model treats the inner atmospheric boundary differently, making it difficult to define input conditions that, once implemented, are identical in all models. Some models form an ionosphere self-consistently from neutral thermospheric and/or exospheric profiles, and some specify the ionospheric state or an ionospheric flux at the lower boundary. For this initial comparison exercise we therefore took the approach of completely specifying the conditions in the upper atmosphere and ionosphere, so that each modeler could choose the most relevant set of inputs for their model, extrapolating if necessary. Differences in the inner boundaries of the models (e.g. altitude, chemical reactions used) should create differences in the model results by creating different relative and total abundances of planetary ions throughout the system. One of the goals of our effort is to evaluate the importance of the choice of lower boundary conditions for determining the structure of the global plasma interaction.

We used simulated outputs from the Mars Thermospheric General Circulation Model (MTGCM) (e.g. Bougher et al., 1999a; Bougher et al., 2000, 2006, 2008), which has been validated and compared extensively with recent accelerometer (e.g. Bougher et al., 1999b, 2006; Bell et al., 2007), radio science (Bougher et al., 2001; Bougher et al., 2004), electron reflectometer (e.g. Lillis et al., 2005), and stellar occultation (McDunn et al., 2009) data sets from Mars. The modern MTGCM is a finite difference primitive equation model that self-consistently solves for time-dependent neutral temperatures, neutral-ion–electron densities, and three component neutral winds over the globe and above ~70 km (see overview in Bougher et al. (2008)). The MTGCM is driven from below by the NASA Ames MGCM code (Haberle et al., 1999) at this 70 km (1.32 microbar) interface. There is a detailed upward coupling between the MGCM and MTGCM across this boundary, which captures migrating plus non-migrating upward propagating tides as well as the thermal expansion and contraction of the Mars lower atmosphere with the passage of the seasons and dust storm events (e.g. Bougher et al., 2004, 2006; Bell et al., 2007).

The MTGCM was run with incident EUV flux corresponding to typical solar moderate conditions at Mars Equinox (the model used an F10.7 index of 130), and altitude profiles for neutral ($O$, $CO$, $N_2$, $CO_2$) and charged ($O_2^+$, $O^+$, electrons) species were extracted as a function of altitude and solar zenith angle (SZA) along an equatorial cut. The altitude profiles extended from 100 to 260 km with 5 km resolution and the resolution in SZA was 5°. Temperature profiles were also extracted.

Sample model outputs extracted from the MGCM–MTGCM simulation which are tailored to this model challenge are illustrated in Fig. 1. The figure shows $CO_2$, O, and electron density and temperature as a function of altitude in the equatorial plane. There are considerable differences between the midnight-to-noon (0–12 h) and noon-to-midnight (12–24 h) sectors. Other SZA slices could be extracted at the noon meridian and over the poles, providing much different variations of the density and temperature fields. This illustrates the asymmetric character of the 3D Mars thermospheric and ionospheric structure that must eventually be addressed by global plasma interaction models.

Mars possesses a substantial extended exosphere and hot corona which influences (and is influenced by) the incident solar wind plasma to large altitudes. No extended exosphere or corona (beyond the MTGCM results, which extend to 260 km) was specified as input for this challenge, and some modeling groups included

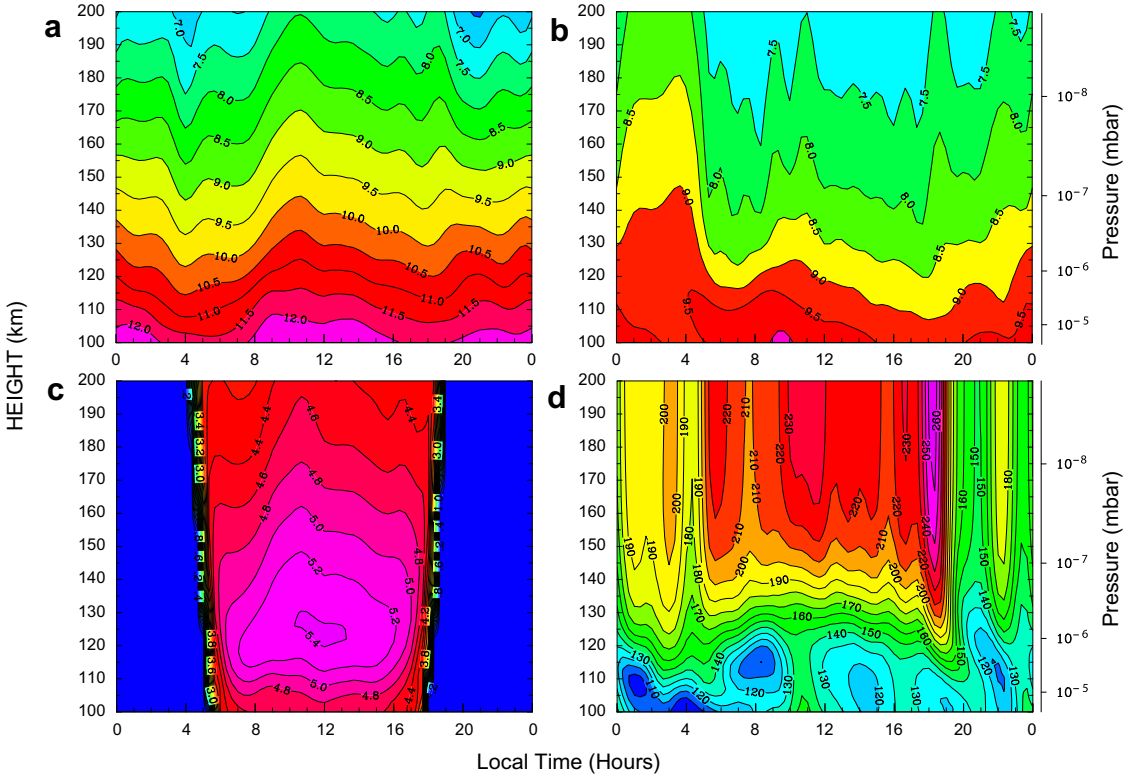


**Fig. 1.** Representative MTGCM results used as atmospheric input for the models, shown as a function of local time in the Mars equatorial plane and altitude. Quantities shown are (a) $CO_2$ density; (b) O density; (c) electron density (photochemical only); and (d) neutral temperature (K). All quantities are expressed in cgs units and the contour intervals are $10^{0.5}$ (a, b), $10^{0.2}$ (c), and 10 K (d).

their own hot exosphere in addition to the MTGCM input while others did not. This may create substantial differences between some model results. We take care in the sections below to point out which modeling groups have excluded the exosphere from the simulation presented here.

For this initial model comparison activity we exclude martian crustal magnetic fields from the simulations. Strong crustal fields (Acuña et al., 1998) have been shown to influence the plasma interaction locally (e.g. Mitchell et al., 2001; Crider et al., 2002; Vignes et al., 2002; Krymskii et al., 2002; Brain et al., 2003; Breus et al., 2005; Gurnett et al., 2005), and perhaps globally (Luhmann et al., 2002; Withers et al., 2005; Brain et al., 2005; Fang et al., in press), and their effects have been considered in global models (Ma et al., 2002, 2004; Harnett and Winglee, 2003, 2006). Crustal fields have two main effects on the plasma environment (Brain, 2006). They contribute magnetic pressure, which perturbs plasma boundaries and shields some portions of the atmosphere from solar wind related ionization processes. They also cause magnetic field topologies that connect the solar wind to the crust, creating vertical ionospheric magnetic fields and allowing exchange of energy and particles between the solar wind and atmosphere. Not all participating simulation groups have incorporated crustal fields into their models. To ensure that all the simulations results would be as directly comparable as possible we have therefore not considered crustal fields at this first stage of the challenge.

## 3. Models

The input conditions described in the previous section were simulated by seven different research groups with models spanning the range of physical assumptions presently used for Mars. All models are 3D, global, and track multiple ion species. Two MHD models participated, one multi-fluid model, and four hybrid models. Since there are multiple models of each type, we refer to them in this paper by the last name of the primary author responsible for running the model and providing results; in many cases several people were involved with these tasks. Table 2 summarizes the key features of the participating models, which we briefly describe below.

The Ma MHD model is developed based on the platform of the BATS-R-US (Block Adaptive-Tree Solar wind Roe-type Upwind Scheme) code (Powell et al., 1999; Tóth et al., 2005). The model calculates the densities of protons (planetary and solar wind protons are not distinguished) and three major ion species ($O^+$, $O_2^+$, and $CO_2^+$) in the martian ionosphere, as well as the magnetic field and combined plasma bulk velocities and energies. The model typically uses a 3D neutral atmosphere specified by the MTGCM, and calculates the upper ionosphere self-consistently based on major chemical reactions including photoionization, recombination, electron impact, and charge exchange processes as well as 10 chemical reactions. Local time-stepping is used, where the time steps in individual cells can change dynamically and differ from each other in order to satisfy the Courant condition locally. This method can significantly reduce the number of iterations needed for convergence, but is only appropriate for a steady state solution. The Ma model is implemented on a spherical grid that extends to large radial distances, and the MHD equations are solved in grid cells from +8 to $-24$ $R_M$ in $x$ and from +16 to $-16$ $R_M$ in $y$ and $z$. Close to the planet the spatial resolution is 10 km in the radial direction and 1.875° in theta and phi coordinates. At higher altitudes the resolution is 600 km and 3.75°. At the inner boundary, the $O^+$, $O_2^+$, and $CO_2^+$ densities are set at the photochemical equilibrium solution. The $H^+$ density is set to 0.3 $cm^{-3}$. More details can be found in Ma et al. (2002, 2004), and Ma and Nagy (2007). The simulation performed for this work used 3D MTGCM results rather than the 2D results presented in Section 2, and a hot oxygen corona was included.

The Terada MHD model uses a finite-volume third order total variation diminishing (TVD) scheme with a monotonic upstream for conservation laws (MUSCL) approach. It tracks 10 ion species ($O^+$, $O_2^+$, $CO_2^+$, $NO^+$, $CO^+$, $N_2^+$, $N^+$, $C^+$, $He^+$, $H^+$), and solves continuity equations for four more species ($H_2^+$, $Ar^+$, $Ne^+$, $Na^+$). The ionosphere is calculated self-consistently from the MTGCM background and includes 94 chemical reactions and collisions. Photoionization, electron impact, charge exchange, and recombination are included. The model has an grid with 3.5–300 km spatial resolution extending out to 10.2 $R_M$, and uses dynamic time-stepping of approximately 0.04 s. More details on this model can be found in Terada et al. (2009a,b).

The Harnett multi-fluid model tracks the individual density, momentum and pressure of three ion fluids (solar wind $H^+$, planetary $H^+$, and $O_2^+$) and one electron fluid, in addition to the magnetic and electric fields using a second order Runge-Kutta method to solve the relevant equations. The inner boundary for the results presented from this model was set at an altitude of 525 km, with the density and temperature of all the ion species held constant at the boundary. At one grid point above the boundary all parameters were allowed to vary as determined by the numerical calculations. The model uses dynamic time-stepping and a cartesian grid system with resolution of 0.4 $R_M$ far from the planet and 42 km at lower altitudes. The simulation area encompassed $-7.9$ $R_M$ on the day side, $+35.6$ $R_M$ downtail, and ±17.4 $R_M$ on the flanks and over the poles. More details on the martian version of this model can be found in Harnett and Winglee (2003, 2006, 2007). For the simulations described in this work, the $H^+$ and $O_2^+$ densities and temperature at the model lower boundary are set to latitudinally dependent values consistent with Viking 1 measurements; the MTGCM atmospheric inputs were not used.

The Brecht ion hybrid model uses a predictor–corrector scheme developed by Harned (1982). It treats three kinetic ion species ($H^+$, $O_2^+$, and $O^+$) and an electron fluid, and treats the ionosphere self-consistently in the same manner as the Ma model, using the same chemistry. An ionospheric conductivity tensor is calculated in the model based on ion neutral collisions, and the electron temperature is calculated self-consistently. The model is implemented on a cartesian grid, and for the simulation presented here had spatial resolution of 250 km (the ionosphere is loaded at much higher resolution) and a time step of .02 s. Further details on the model and numerical methodology can be found in Brecht (2006, 2009),

**Table 2**
Participating models and their characteristics for this study.

| Model | Resolution | Time step | Lower boundary (km) | Hot exosphere | Differences from specified inputs |
|---|---|---|---|---|---|
| Ma (MHD) | 10–600 km | Local | 100 | Yes | 3D MTGCM inputs |
| Terada (MHD) | 3.5–300 km | Dynamic | 100 | No | |
| Harnett (multi-fluid) | 42 km – 0.4 $R_M$ | Dynamic | 250 | No | Tracks $O_2^+$; used Viking 1 instead of MTGCM |
| Brecht (hybrid) | 250 km | .02 s | 0 | No | 425 km/s solar wind; IMF flipped |
| Kallio (hybrid) | 180–720 km | .02 s | ~210 | Yes | Approximated MTGCM |
| Modolo (hybrid) | 131 km | .03 s | 100 | Yes | |
| Boesswetter (hybrid) | 50–165 km | .07 s | 120 | Yes | Approximated MTGCM |

Ledvina and Brecht (submitted for publication), Brecht (1997), Brecht and Thomas (1988). The simulation run presented here used a slightly different IMF (had opposite polarity) and solar wind speed (425 km/s instead of 400 km/s) than specified for the comparisons.

The Kallio ion hybrid model is a standard quasi-neutral hybrid model where ions are modeled as particles and electrons form a massless, charge neutralizing fluid. It treats five kinetic ion species (solar wind $H^+$, ionospheric $O^+$ and $O_2^+$, and exospheric $O^+$ and $H^+$) and an electron fluid. The electron density altitude profile used in the model was an analytical function of SZA derived from MTGCM results. The model includes an isothermal electron pressure. The grid is cartesian, with smaller cell size close to the planet, and extends from −14,400 to +14,400 km in $x$, $y$, and $z$. Like the Harnett model an ion production rate is specified at the lower boundary, set at ~210 km. More information on this model can be found in Kallio et al. (2008, 2009), Kallio and Janhunen (2003). This simulation includes a neutral hydrogen and oxygen corona with production rates and scale heights consistent with the results of Barabash et al. (2002).

The Modolo ion hybrid model is based on the 'Current Advance Method and Cyclic Leapfrog' algorithm designed by Matthews (1994), now frequently referred to as CAM-CL. It treats six kinetic ion species (solar wind $H^+$ and $He^{++}$, planetary $H^+$, $O^+$, $O_2^+$, and $CO_2^+$) and an electron fluid. The electron fluid is assumed to be adiabatic with a polytropic index equal to two (the fluid models use 5/3), with two specified temperatures for the undisturbed solar wind plasma and the ionospheric plasma. Planetary ions are produced by three processes: photoionization, charge exchange, and electron impact. The local production rate of each ion species is computed from the assumed neutral reservoirs of atomic oxygen, hydrogen, and carbon dioxide and the self-consistent dynamics of the ions by using model cross sections or ionization frequencies. In addition, 10 chemical reactions are included to describe the lower ionosphere. The model is implemented on a uniform cartesian grid with cubic cells, extending from −2.4 to 3 $R_M$ in $x$ and from +5 to −5 $R_M$ in $y$ and $z$. More information on this model can be found in Modolo et al. (2005, 2006), Modolo and Chanteur (2008). This model used an extended neutral corona of atomic hydrogen and oxygen.

The Boesswetter ion hybrid model is a standard 3D code that operates on an arbitrary curvilinear grid. It treats two kinetic ion species ( $H^+$ and $O^+$) and an electron fluid. A gradient electron pressure term and neutral drag terms are included. A constant solar UV radiation yields the dayside ion production function in the form of a Chapman layer for atmospheric ions which depends on both altitude and solar zenith angle. Nightside production is assumed to be independent of the solar zenith angle. The grid has a 50 km curvilinear (fish-eye) configuration close to the planet enabling spatial resolution of .05 $R_M$, and has a 165 km regular cartesian configuration at higher altitudes. Ions hitting the lower boundary at 120 km altitudes are removed from the simulation, but electric and magnetic fields are solved everywhere (outside and inside the obstacle). More information on this model can be found in Boesswetter et al. (2004), Simon et al. (2007), Boesswetter et al. (2007, 2009). This model does not use the full 2D MTGCM results, and instead uses the MTGCM subsolar oxygen density profile to create a spherically symmetric atomic oxygen cloud around Mars. A hot oxygen exosphere is included in this model.

The deviations of each of the model inputs from the specified input conditions are described above, but are worth summarizing since they represent additional reasons why the model results may differ. Four models (Ma, Kallio, Boesswetter, and Modolo) used an extended neutral corona in addition to the colder neutrals dictated for lower altitudes. Two models deviated from the MTGCM inputs at the lower boundary (Ma used 3D rather than 2D results, and Harnett used Viking 1 results), though at least two other models approximated the MTGCM results in some way (Kallio and Boesswetter). And the Brecht model was run for upstream conditions that were similar but not identical to those specified for this challenge.

## 4. Subsolar pressure partitioning

The models were run using the input conditions described in Section 2, and the results were compared in three ways. First, we extracted samples of dynamic, thermal, and magnetic pressure along the subsolar line in order to determine whether total pressure is conserved in each model and how pressure is partitioned. It has long been assumed that pressure is conserved in a Mars or Venus-like plasma interaction, with solar wind dynamic pressure dominating upstream from the shock, thermal pressure dominating in the magnetosheath, and magnetic and/or ionospheric thermal pressure dominating closer to the planet (Zhang et al., 1991; Crider et al., 2003). Pressure conservation at Mars has only recently been demonstrated observationally, using measurements from Mars Express (Dubinin et al., 2008). This same work demonstrated that magnetic pressure can exceed ionospheric thermal pressure to low altitudes. These observations present a challenge for future modeling efforts because many models do not allow magnetic field to penetrate the lower ionosphere.

The pressure terms for each model are shown in Fig. 2. As expected, dynamic pressure dominates far from the planet (with magnitude of ~0.8 nPa corresponding to the specified input conditions). Most models have an intermediate region where thermal plasma pressure (with contributions from both solar wind and planetary plasma) is the dominant term and all models have a lower altitude region where thermal pressure decreases as magnetic pressure increases. The figure shows a number of substantial differences between the results as well.

The two MHD models produce generally similar results, especially when compared with the results from the other models. Both models show a sharp transition from dynamic to thermal pressure at the model bow shock and a more gradual transition from thermal to magnetic pressure at lower altitudes near the bottom of the magnetosheath. Narrow shocks (with thickness of one computation cell) are characteristic of fluid models. At very low altitudes thermal pressure is dominant for these two models since they both include a self-consistent ionosphere as part of the model calculation. The results from the two models differ in some details. The transition from dynamic to thermal pressure for the Terada model occurs nearly 400 km lower than for the Ma model, and the transition from thermal to magnetic pressure occurs at slightly lower altitude as well. The region dominated by magnetic pressure is broader in the Ma model, and has larger peak magnitude. These differences might be explained by the inclusion of a hot oxygen corona in the Ma model. Addition of sufficient exospheric ions to the plasma flow should add thermal pressure and decrease dynamic pressure, contributing to higher plasma boundaries. However, Ma et al. (2002) found that inclusion of a corona did not significantly alter boundary locations, and Brecht (2009) found that inclusion of a corona moves boundary locations to slightly lower altitudes near the flanks of the interaction. Another difference between the two models is that the Ma model used 3D (rather than 2D) MTGCM results. It is unclear whether or how these two differences in model inputs account for the different results in Fig. 2, or whether the details of the simulation method are responsible. The reason for these differences can be investigated in future comparisons by running identical inputs for both models and comparing to the results presented here.

The remaining models produce substantially different results from the single fluid MHD models, and from each other. We note three main differences. First, all models exhibit a more gradual

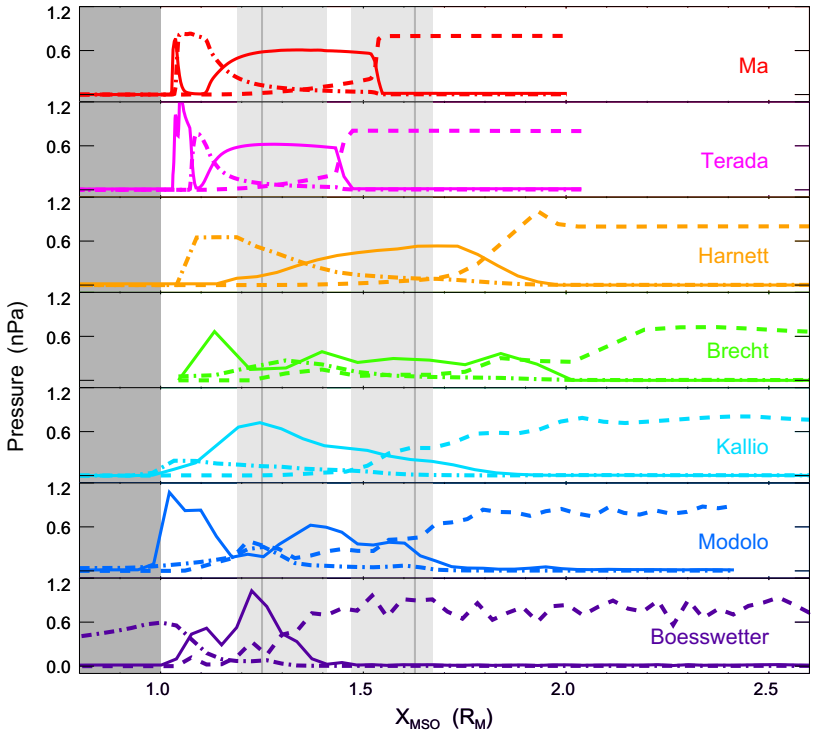


**Fig. 2.** Pressure profiles for the seven participating models, extracted along the subsolar line. Dashed lines indicate dynamic pressure, solid lines indicate plasma thermal pressure, and dot-dashed lines indicate magnetic pressure. The darker shaded area denotes regions interior to the planet. The best-fit MPB and bow shock derived in Trotignon et al. (2006) are indicated by vertical gray lines, and the ranges of best-fit boundary locations based on all previously published work are indicated by the light gray shaded areas. Several simulation results do not include exospheric effects.

decline in plasma dynamic pressure (more than can be accounted for by the generally lower spatial resolution of these models) than the single fluid MHD models. This is almost certainly a result of the physics included in the models. The separate ion fluids in the Harnett model may create broader transitions than the Ma and Terada models. And hybrid models contain ion kinetic effects; shocks form from reflected ions with large gyroradius, and are necessarily broad. The hybrid models also exhibit greater cell-to-cell variation in each pressure term due to the non-fluid behavior of the ion species contributing to those pressure terms. One can distinguish greater cell-to-cell variation for the hybrid models with finer spatial resolution.

Second, the locations of the transition from dynamic to thermal pressure and from thermal to magnetic pressure vary greatly between models. It will be difficult to determine the root cause of these differences until all models are running identical input conditions, but we can rule out a few possibilities in each case. For example, the Harnett model has higher transitions than the MHD models, which may result from the use of multiple fluids, or the use of different inputs for the lower boundary. But the absence of a hot exosphere is not likely to be important for this comparison, since neither the Harnett (higher transitions than Ma) nor Terada (lower) models include one. The decline in dynamic pressure in the Brecht model is very gradual and begins at much higher altitudes than for other models, and no pressure term is clearly dominant in the interaction region above the low altitude ionosphere. The Brecht model includes similar ion chemistry to both the Ma and Modolo models and similar physics to the other hybrid models, so these should not be the reason for these features. The Kallio and Modolo models produce transitions from dynamic to thermal pressure that are similar to the Ma model (which also includes a hot corona), but the low altitude decline in thermal pressure occurs in very different locations. The Boesswetter model has distinct regions dominated by dynamic, thermal, and magnetic pressure. However, the transitions between regions occur much closer to the planet than for most other models. As will be discussed in Section 5, lower ion production for this model may result in boundary locations closer to the planet. Fig. 2 shows that magnetic field is allowed to diffuse into the planet in this model.

Finally, only two of the models (Harnett and Boesswetter) can be said to have a region where magnetic pressure is clearly dominant over other pressure terms. The reason for this is unclear, but should be investigated in future comparisons at a variety of locations since the martian plasma environment clearly has regions that are dominated by magnetic pressure (Dubinin et al., 2008).

The nominal bow shock and Magnetic Pile-up Boundary (MPB) locations calculated from observations are shown in Fig. 2 for reference. Shaded areas show the range in all published subsolar locations of the plasma boundaries (Dubinin et al. (2006), Edberg et al. (2008); and all references in Tables 1 and 2 of Trotignon et al. (2006)). All published shapes for the plasma boundaries use a fitting technique similar to that first proposed by Slavin and Holzer (1981). There is considerable scatter in the published fits, which span many spacecraft missions and decades of observation. Three recent studies might be considered to be especially reliable because they incorporate fits to large numbers of observations (Trotignon et al., 2006; Edberg et al., 2008), to observations from multiple missions (Trotignon et al., 2006), and to MPB crossings close to the subsolar point (Dubinin et al., 2006). The fits from (Trotignon et al., 2006) are shown in the figure for reference. Statistical analysis of these boundaries by a number of authors has found that they respond to a number of different drivers (see Brain, 2006; Edberg et al., 2008), so that there is no guarantee that the locations shown in the figure are appropriate for the input conditions used for this exercise. However, the input conditions that we chose are moderate in every respect, so the modeled boundary locations might be expected to be close to their average observed position. We note that plasma boundary locations are not

observationally determined based on pressure, but we expect a decrease in dynamic pressure at the bow shock and in increase in magnetic pressure at or near the MPB. Three models that incorporated a hot exosphere (Ma, Kallio, Modolo) calculate that the transition from dynamic to thermal plasma pressure occurs within the range of published bow shock locations, while three others (Terada, Harnett, Brecht) did not include a hot exosphere so should not be compared directly to observations. Only one model that included a hot exosphere (Modolo) calculated a transition from dynamic to thermal pressure within the range of published MPB locations, though two other models that lacked a hot exosphere (Harnett, Brecht) also calculated that magnetic pressure becomes the dominant pressure term within this range. All other models calculate a transition from thermal to magnetic pressure at lower altitudes.

One striking feature of Fig. 2 is that the two MHD models both predict a more compact interaction region near the subsolar point than is inferred from observations. There are several possible explanations. First, there are relatively few observations near the subsolar point, so that many of the published fits to existing data could be in error in this region. Second, crustal fields and their effects have been excluded from both MHD models but cannot be excluded from observations. Crustal fields have been demonstrated in observations to have a weak influence on bow shock location, raising its altitude locally (Edberg et al., 2008). Further, Ma et al. (2004) demonstrated that their model provides a better fit to the bow shock location when crustal fields have been included. Finally, both MHD models use a polytropic index of 5/3, which may not be appropriate for the plasma interaction at Mars. Previous fluid studies of the martian bow shock have shown that the adiabatic index has a large impact on the strength and location of the bow shock (Spreiter et al., 1966; Slavin and Holzer, 1983).

Fig. 2 shows great diversity in the variation along the subsolar line of the different pressure terms. A good test of the models, however, is whether the total pressure is constant when the dynamic, thermal, and magnetic pressure terms are summed. Since the models have nominally reached 'steady state', this pressure balance should at least approximately hold. Fig. 3 shows the total pressure along the subsolar line for each model. Most of the models show that pressure is conserved, with a few deviations from the nominal total pressure of 0.8 nPa. The profiles for the MHD models are very smooth, while the profiles for the models that track individual ion species separately have more cell-to-cell variation. The Brecht model does not appear to conserve pressure throughout the interaction region, and the decrease in dynamic pressure is not compensated by commensurate increases in thermal or magnetic pressure close to the planet. There is a great deal of scatter in the total pressure for this model as well. The Kallio and Harnett models also show a small decrease in total pressure in the region dominated by thermal plasma pressure. There are several possible explanations for the observed decrease in total pressure, including physical, computational, and model error or numerical deficiencies. First, pressure need not be conserved in the plasma quantities. For example, the Brecht model includes ion neutral collisions which may remove energy from the shocked solar wind plasma, causing a decrease in total pressure at lower altitudes. However, the Boesswetter model includes neutral drag terms as well and appears to conserve pressure. Next, calculation of thermal pressure from a hybrid model requires sufficient numbers of particles in each cell to accurately compute a temperature. Additionally, thermal pressure can be computed as a tensor directly from the particles by comparing the velocity of individual particles to the local mean particle velocity, or by assuming an isotropic Maxwellian distribution and computing temperature from the particle velocities. It is possible that the different hybrid models computed thermal pressure in different (non-comparable) ways, or that some models have too few particles per cell to compute thermal pressure reliably. Other deviations from pressure conservation apparent in the figure are the excess of pressure close to the planet in the Ma, Terada, and Modolo models—all of which include an ionosphere produced within the simulation that explains the excess. And the Boesswetter model has an unexplained excess of thermal pressure outside of 1.2 $R_M$.

## 5. Noon–midnight particle densities

Two-dimensional cuts of solar wind $H^+$ and planetary $O^+$ density were extracted in the noon–midnight plane for each model and compared. The results are shown in Figs. 4 and 5. There are a number of notable similarities and differences between the models. Here we limit ourselves to discussion of the size and asymmetry in the plasma boundaries apparent in the figures, and the pathways for escape of planetary ions. Each of these topics has been frequently addressed by spacecraft observations and in the literature.

The location of the model bow shock is apparent from the plots of hydrogen densities, which increase from their upstream values of 3 $cm^{-3}$ to values greater than 10 $cm^{-3}$ within 1–2 $R_M$ of the planet. On the day side, the solar wind proton density decreases again at the lower boundary of the magnetosheath, often described as the Induced Magnetosphere Boundary (IMB) or protonopause. The shape determined for the IMB based on observations is highly

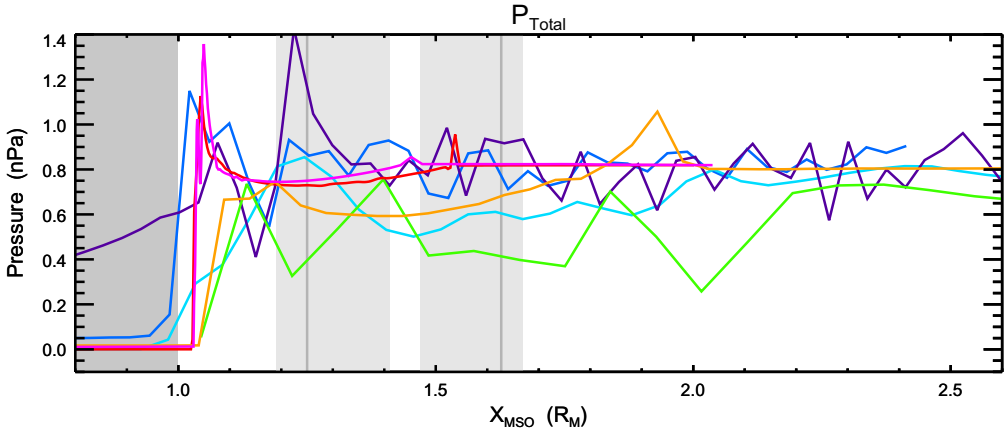


**Fig. 3.** Total pressure along the subsolar line for each of the participating models. The sum of dynamic, thermal, and magnetic pressure is shown using the same color scheme for each model as in Fig. 2. Best-fit boundary locations based on observations are shown in the same style as Fig. 2.

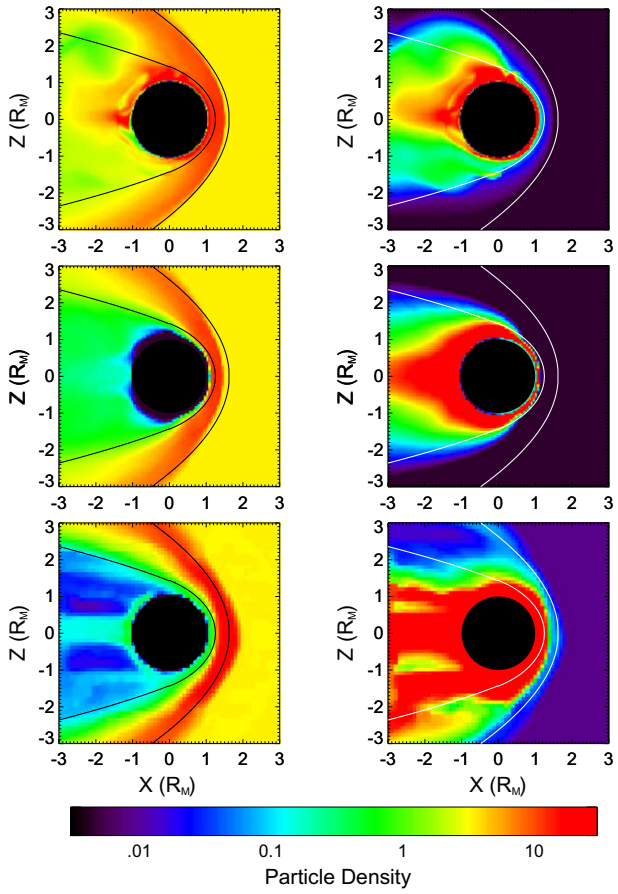


**Fig. 4.** Two-dimensional cuts of $H^+$ (left) and $O^+$ (right) in the noon–midnight ($y = 0$) plane. Results are shown for the Ma, Terada, and Harnett models from top to bottom. The nominal locations of the bow shock and MPB from (Trotignon et al., 2006) are indicated in black in each panel. Several simulation results do not include exospheric effects.

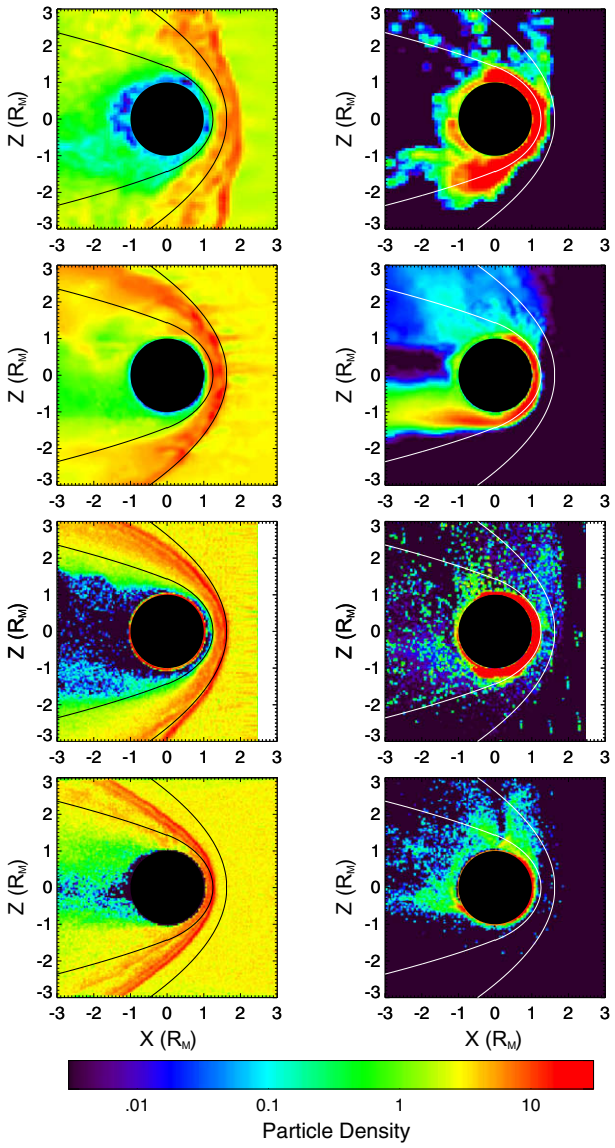


**Fig. 5.** Model results for the Brecht, Kallio, Modolo, and Boesswetter models, from top to bottom, using the same format as for Fig. 4.

similar to the shape of the MPB, which is determined based on magnetic field and electron observations (Trotignon et al., 2006), and they are likely to be the same boundary recognized in different particle and field measurements. Bow shock and MPB positions at Mars and Venus are influenced by such drivers as solar wind pressure, crustal field locations, and IMF direction (e.g. Russell et al., 1988; Zhang et al., 1991; Brain, 2006; Edberg et al., 2008 and references therein). IMF direction, in particular, creates an asymmetry in the boundary shapes in the plane of the solar wind convection electric field ($\vec{E}_{SW}$) (Russell et al., 1988; Zhang et al., 1991; Vignes et al., 2002; Brain et al., 2005). For the input conditions chosen here (IMF in the ecliptic with a $+y$ component) $\vec{E}_{SW}$ points in the $+z$ direction so that any asymmetry in the simulations should be readily apparent in a noon–midnight cut.

From the plots of $H^+$ density in Fig. 4, the boundary locations for the two MHD models are fairly similar. Note these two models do not distinguish between solar wind and planetary $H^+$. Both the Ma and Terada model calculate a shock location that is closer to the planet near the subsolar point and flares more than the fits to observations. Fits to boundary locations determined from MGS and Phobos 2 observations by Trotignon et al. (2006) are not reliable near the subsolar point due to the orbit geometry of the spacecraft. The inclusion of an exosphere in the Ma model may lead to higher boundary locations than for the Terada model, as discussed in Section 4. The Ma model does not track solar wind and planetary protons separately, and the low altitude and nightside proton densities are larger than for any other model. The Terada model shows that solar wind proton densities drop by an order of magnitude or more at the lower boundary of the magnetosheath. The Terada model results are perfectly symmetric (a natural result of the MHD calculation), while the Ma results show small but unexpected asymmetry in the boundary locations and large asymmetry at low altitudes that are suggestive of the Kelvin–Helmholtz instability operating in one hemisphere of the planet. However, the Ma model used three-dimensional input from the MTGCM at low altitudes, rather than the two-dimensional input used by the other models, which may explain the asymmetry.

The Harnett multi-fluid model results for $H^+$ are qualitatively similar to the MHD results, with a few notable differences. First, the bow shock is less flared than for the single fluid MHD models and is located exterior to the Trotignon et al. (2006) bow shock. This difference maybe attributed to the different ionosphere used by this model, the additional planetary ions included in the solar wind for model stability (evident in the plot of $O^+$ density), or the use of multiple fluids. Next, the multi-fluid approach allows for an asymmetric magnetic pile-up boundary shape, which is closer to the planet than the fit in the $+z$ hemisphere and farther in the $-z$ hemisphere. Proton densities drop two orders of magnitude or more in some locations behind the planet.

The hybrid models show a great deal of variability in $H^+$, but share a few common features not evident in the MHD models. The shock for the Kallio and Modolo models agrees quite well with the fit to observations. The shock for the Brecht model forms far from the planet and is highly flared, while the shock for the Boesswetter model forms very close to the planet with flare angle matching the fit to observations. One can see from the $O^+$ panels that the oxygen density for the Boesswetter model is at least an order of magnitude lower than the other hybrid models close to the planet. This low planetary ion density, possibly resulting from inclusion of only a single ion production process with low rate, should reduce the size of the solar wind obstacle, making the boundaries form closer to the planet. The Brecht model used an upstream proton density lower than 3 $cm^{-3}$. Wave-like density structures are seen in the shock and magnetosheath of the Modolo and Boesswetter models, which have fine spatial resolution. Solar wind proton densities drop below the magnetosheath and in the wake of the planet, with a drop of 3–4 orders of magnitude behind the planet for the Modolo model.

The plots of $O^+$ density in Figs. 4 and 5 indicate the dominant pathways for escaping planetary ions under the assumptions of each model. A number of processes are theorized to remove planetary ions from the martian atmosphere, including ion pickup by $\vec{E}_{SW}$, bulk ionospheric removal processes such as stripping via Kelvin–Helmholtz instabilities at the top of the ionosphere or reconnection, and possible removal via ion outflow processes. The relative importance of these processes is a necessary component to understanding atmospheric escape to space at Mars and similar bodies. However, distinguishing ions removed by each process in observations or in model results can be difficult. The pathways that are used by the ions as they escape can help to constrain the different processes.

Both MHD models indicate that the central magnetotail is the main channel through which planetary ions are lost under the MHD assumption, and that ion densities decrease with increasing distance (in $z$) from the central tail. This central tail outflow is a result of the treatment of the pickup ions as a fluid, which may or may not be physically appropriate. However, MHD has been found to describe many systems where kinetic effects are known to be present—perhaps because of the ion gyromotion scale or perhaps because of effective ion scattering processes in the system. $O^+$ extends to higher altitudes on the day side in the Ma model, which is expected since a hot oxygen corona was included for this model run. This model also shows considerable asymmetry near the flanks, with much higher densities in the $+z$ hemisphere.

The dominant pathway for escaping oxygen in the multi-fluid model is the central magnetotail, as for the MHD models. However, the region over which this escape occurs is fairly broad at $-3$ $R_M$, and there is some indication that there are multiple channels within the magnetotail for escaping oxygen. Asymmetry results from the use of an expanded Ohm's law in the model equations (including a Hall term) and the use of separate ion fluids, each with its own bulk velocity and temperature. We note here that the Harnett model does not track $O^+$, so results for $O_2^+$ are presented instead. $O_2^+$ has greater mass (and therefore larger gyroradius) than $O^+$, so that any ion kinetic effects approximated by the multi-fluid technique should be more pronounced than for the hybrid model results for $O^+$.

All four hybrid models show similar pathways for oxygen ion escape that differ from the MHD results. All show some fraction of ions escaping in the $-z$ hemisphere of the central tail region, and a second feature originating in the low altitude flanks of the $+z$ hemisphere and extending to high altitudes. These are interpreted to be low energy oxygen escaping either via low energy ion pickup or ion outflow in the $-z$ hemisphere, and a higher energy 'pickup ion plume' or 'fountain' in the $+z$ hemisphere (Fang et al., 2008). Measurements of escaping ions from Mars Express and Venus Express show asymmetries in escaping particle flux and energy organized by the solar wind electric field, similar to those shown here for the simulations (Barabash et al., 2007a,b; Fedorov et al., 2008).

The hybrid models all show a north–south asymmetry in the plots of $O^+$ and $H^+$ density, indicating an apparent influence of the solar wind convection electric field on ion motion in the martian system. This asymmetry is well discussed in the literature for planetary ions, which are accelerated in the direction of positive electric field. Therefore, planetary ions extend to higher altitudes in the $+z$ hemisphere, as seen in the figures. Given that the incident plasma flow is mass-loaded preferentially in the $+z$ hemisphere, one might expect the plasma boundaries in that hemisphere to form at higher altitudes as well. However, the figures demonstrate that this is not the case; the bow shock and magnetosheath are found at lower altitudes in the $+z$ hemisphere, so that the sense of the asymmetry is opposite that of the planetary ions. The sense of this asymmetry has been noted in previous hybrid simulation results (Brecht and Ferrante, 1991; Kallio and Janhunen, 2001, 2002; Boesswetter et al., 2004; Modolo et al., 2005; Simon et al., 2007), and in observations (Brain et al., 2005; Brain, 2006). Simon et al. (2007) are able to explain the sense of the asymmetry for the Ion Composition Boundary (analogous to the MPB/IMB) by considering the Lorentz forces acting on solar wind and ionospheric particles. Brecht and Ferrante (1991) explains the sense of the asymmetry via multiple interactions of solar wind ions with the magnetic barrier region, and Hall currents at the MBP, and suggests based on simulations that the sense of the asymmetry should be different for $H^+$ at Venus, possibly because of the smaller ratio of magnetospheric scale size to ion gyroradius for Venus. Finally, Kallio and Janhunen (2001) showed that the precipitation of $H^+$ to the upper atmosphere is more intense on the $+E_{SW}$ hemisphere than on the opposite $-E_{SW}$ hemisphere. Noting that $H^+$ ions are accelerated in the $-E_{SW}$ direction while $O^+$ ions are accelerated in the opposite $+E_{SW}$ direction, Kallio and Janhunen (2002) suggest that these opposite ion motions are a manifestation of a sort of conservation of the total ion momentum along the $z$ direction.

## 6. Escape rates

Most models have published estimates of the total atmospheric ion escape flux, and the variation in this flux for different conditions. In order to extrapolate to earlier epochs in martian history, when atmospheric escape rates are assumed to have been much higher, the models are then either run for extreme conditions (Harnett and Winglee, 2006; Ma and Nagy, 2007; Brecht and Ledvina, 2006; Terada et al., 2009a), or the variation in escape rates for conditions relevant to the present epoch are extrapolated backward in time Barabash et al. (2007a). While the pathways and processes that contribute to the total escape flux under a given set of conditions are critical for understanding the physics relevant for escape, the total escape flux predicted by all the models for a single set of input conditions provides a useful constraint on the uncertainty associated with such calculations.

Table 3 shows the total $O^+$ escape rate from each simulation for the case studied here. The Harnett model does not track $O^+$, so the escape rate for $O_2^+$ is shown instead. Observed escape rates for $O^+$ from Mars range from $5 \times 10^{24} - 3 \times 10^{25}$ $s^{-1}$ measured during solar maximum by the Phobos 2 spacecraft (Lundin et al., 1990; Verigin et al., 1991), to $1.6 \times 10^{23} - 3.3 \times 10^{24}$ $s^{-1}$ measured during solar minimum conditions by Mars Express (Barabash et al., 2007a; Lundin et al., 2008). The values reported in Table 3 for solar moderate conditions are generally intermediate between these two ranges. All models exclude the effects of crustal fields, which

**Table 3**
Modeled $O^+$ escape rates for each model in units of $10^{24}$ $s^{-1}$. The Harnett model tracks $O_2^+$ instead.

| Ma | Terada | Harnett | Brecht | Kallio | Modolo | Boesswetter |
|---|---|---|---|---|---|---|
| 6.9 | 1.0 | 18 | 6.5 | 2 | 1.3 | 6.3 |

have been shown to lower the modeled ion escape fluxes in some situations when they are incorporated (Ma et al., 2002; Harnett and Winglee, 2006; Fang et al., in press). Further, several of the models did not include an extended exosphere in their calculations. Both of these omissions in the model results presented here should lead to lower ion loss rates, and also make it difficult to compare directly to quantities measured in the presence of an exosphere and crustal fields.

More important than the absolute loss rate for this comparison activity are the relative differences in escape rates between the models. The escape fluxes vary by more than an order of magnitude, from $1.0 \times 10^{24} - 1.8 \times 10^{25}$ $s^{-1}$. We note that the highest estimate, from the Harnett model, is for $O_2^+$ and not $O^+$, so may not be directly comparable to the others. However, Carlsson et al. (2006) and Barabash et al. (2007a) found from Mars Express observations that $O_2^+$ and $O^+$ escape at approximately the same rate. We might expect the value in Table 3 for the Harnett model to be even higher, since the model has previously calculated ~10–20% higher escape rates for $O^+$ than $O_2^+$ (Harnett and Winglee, 2006). The additional planetary oxygen upstream of the bow shock for this model, evident in Fig. 4, is likely also related to the larger escape rate. Regardless, the difference in modeled escape rates is an order of magnitude or more. We caution that identical conditions were not run for each model; some included a hot exosphere while others did not. The influence of the exosphere should certainly be examined in a future comparison. For now we note that both the highest and lowest escape rates were from models where the exosphere was not considered, suggesting that the variations from model to model may be more important in creating the differences in Table 3 than whether the exosphere was included.

The variation in ion loss rates might be viewed as fairly small, given differences of several orders of magnitude in planetary ion density at a given location in Figs. 4 and 5. In this view, one might infer that similar amounts of material leave the system in each model, via different pathways. The discrepancy may also be viewed as fairly large when one considers that the models were run for similar input conditions, and that these models are used to extrapolate to earlier epochs during times of more extreme and uncertain input conditions. In this view, one should infer that the application of global plasma models to constrain atmospheric escape over martian history has very large associated uncertainties, and that the integrated loss derived from model results may be incorrect by several orders of magnitude even without considering added uncertainties in the solar, planetary field, and early atmosphere histories.

## 7. Discussion

Seven global plasma models for Mars were run for the same set of input conditions, and the simulation results were compared to each other in three ways. One-dimensional samples of dynamic, thermal, and magnetic pressure were extracted along the subsolar line to determine how pressure is partitioned and conserved in each model. Two-dimensional samples of $H^+$ and $O^+$ ion density in the plane of the asymmetry created by the solar wind convection electric field were extracted to determine the location and asymmetry of plasma boundaries and the pathways of escaping planetary ions. The total escape rate for $O^+$ was extracted from each model to determine variation in calculated loss rates for moderate conditions in the present epoch.

From this exercise we find that MHD models are characterized by sharp transitions in pressure and ion density near plasma boundaries, and that the dominant pathway for escape is in the central magnetotail region. As noted earlier, this is due to the fluid treatment of the ions in these models, which may or may not mimic reality. Hybrid model results, which contain ion gyroradius effects, are characterized by broad transitions in pressure and density near plasma boundaries, and escape occurs in one hemisphere of the magnetotail and in a large gyroradius 'pickup ion plume'—both controlled by $\vec{E}_{SW}$. The ion motions in these cases resemble those of test particle ions in the MHD flows and fields (e.g. Fang et al., 2008). There is better agreement on the structure of the interaction region between the MHD models than between the hybrid models, despite the fact that one model included a hot oxygen corona and one did not. Significant differences exist between all model results. No single model provides a best match to statistical observations. For some models, the locations of plasma boundaries and transitions between dominant pressure terms suggest that there may be problems in the model itself, the implementation of the input conditions, or the extraction of the diagnostic quantities used for comparison here. More than an order of magnitude difference in $O^+$ escape rates (for similar input conditions) suggests that published estimates of absolute escape rates from models should be regarded cautiously until their accuracy has been examined more thoroughly. The variation in escape rates may be partially due to the inclusion of an extended exosphere in three of the models. Because of this idealized nature of the specified case study, we do not present detailed comparisons with observations (e.g. along an orbit trajectory) at this time. Such comparisons have been made for the individual models, but no two model results have been compared to the same set of spacecraft data. We plan to make such comparisons in a subsequent model challenge activity.

While the model results are similar in many ways, the many differences provide a good opportunity to better understand the models and the physics operating at Mars. There are many possible reasons for the different model results. We believe that the two most important of these are the limiting physical assumptions of the models (MHD, multi-fluid, hybrid) and the manner in which atmospheric/ionospheric/exospheric conditions are implemented. All models implement the upstream solar wind conditions in the same manner and without difficulty. However, the atmosphere and lower boundary are treated differently by all models, and it will take further work to verify that each model has implemented an equivalent lower boundary. Even those models that included a hot exosphere in their calculations implemented it differently, so that it is not surprising that the simulation results (e.g. Figs. 4 and 5) are so different. In our opinion, this work demonstrates the importance of the martian atmosphere and crustal fields (not included here) in determining the structure of the global interaction region. However, other possible reasons for differences in the results likely contribute and should be investigated. These include the model time step and grid relative to the relevant length and timescales for the interaction, time variability in the system (especially for the hybrid models), and model error. Plasma boundaries in the models were compared to statistically determined fits to observed plasma boundaries, with varying success. Differences when comparing model results to statistical observations can result from the fact that the observations represent an ensemble of input conditions while the model results are calculated for a single set of input conditions.

Determination of which models are most appropriate for investigation of the martian system should not be made until future model comparisons where all models are run for exactly the same

input conditions in the atmosphere, ionosphere, and exosphere, and until the model results can be compared in detail to individual spacecraft observations. However, a few things are evident already from the comparisons presented here. First, models which include the kinetic motion of ions (such as hybrid models) are more appropriate for investigating the pathways utilized by escaping atmospheric ions. We infer this from the fact that escaping $O^+$ in the model results qualitatively resembles escaping ion measurements from Mars Express. Next, hybrid models are more appropriate for investigating asymmetry in the interaction region in the plane of $\vec{E}_{SW}$, since no asymmetry resulting from ion motion is possible in an MHD model unless the Hall term is included. Third, the more complex hybrid models have larger grid cell sizes, and have considerable variation in their results. The simpler and computationally less expensive MHD models may be more useful for investigating the interaction region at high spatial resolution, especially at low altitudes where the fluid approximation is better justified. The different physics included in MHD and hybrid models make it straightforward to identify which class of model is appropriate for a given task. More important will be identification of which models from within each class are most appropriate for given investigations, and should be possible after the models have been run for identical conditions.

We view the activity presented here as a first step in a community-wide comparison of model results for Mars, with much work that could and should still be done. A number of interesting questions that should be investigated have presented themselves as a result of this work. Examples include: the role of the extended exosphere in controlling ion escape rates and determining the structure of the interaction region; whether crustal field effects are global or local in nature; and how thermal pressure is computed from hybrid model results. Here we have identified where model results differ and listed possible explanations; in the future we intend to identify the reasons for differences in the model results, first by verifying that the neutral atmosphere, ionosphere, and extended exosphere) are implemented equivalently in each model. Several more comparisons could be made, including additional pressure (away from the subsolar point) and density (in the tail or equatorial planes) samples from the models, investigation of the predicted magnetic and electric fields, more detailed investigation of ion production and escape rates for several species, and more detailed comparisons with spacecraft data (both statistical results and observations from individual orbits). More input conditions could be run in order to probe the response of the martian system to different input conditions such as solar cycle and seasonal effects, or the plasma environment at ancient Mars. Use of a variety of models for this purpose would allow us to determine whether the relative changes seen in a single model as input conditions are varied are reproduced in other models as well. Crustal field effects should be investigated once more models have incorporated them. And time variability in the system could be studied for a given set of input conditions. Given all of these possible investigations, we plan to continue this effort as long as interest persists in the community of scientists interested in understanding the interaction of solar wind plasma with the martian atmosphere.

## Acknowledgments

This work resulted from the generous cooperation of the martian modeling and observational community, and was first presented at the SWIM (Solar Wind Interaction with Mars) Chapman Conference held in San Diego in January of 2008. The authors thank three reviewers for constructive comments that substantially improved the manuscript. D.A.B. thanks the modelers for selfless contributions of effort and results which made these comparisons possible. Portions of this manuscript were completed with support from ISSI International Team #142. D.A.B. performed work under NASA Grant NNX06AD97G.

## References

Acuña, M.H., and 19 colleagues, 1998. Magnetic field and plasma observations at Mars: Initial results of the Mars Global Surveyor mission. Science 279 (March), 1670–1676.

Barabash, S., Holmstrom, M., Lukyanov, A., Kallio, E., 2002. Energetic neutral atoms at Mars 4 Imaging of planetary oxygen. J. Geophys. Res. 107. doi:10.1029/2001JA000326.

Barabash, S., Fedorov, A., Lundin, R., Sauvaud, J., 2007a. Martian atmospheric erosion rates. Science 315 (January), 501–503. doi:10.1126/science.1134358.

Barabash, S., Fedorov, A., Sauvaud, J., Lundin, R., 2007b. The loss of ions from venus through the plasma wake. Science 450 (January), 650–653. doi:10.1038/nature06434.

Bell, J.M., Bougher, S.W., Murphy, J.R., 2007. Vertical dust mixing and the interannual variations in the Mars thermosphere. J. Geophys. Res. 112, E12002. doi:10.1029/2006JE002856.

Birn, J., Drake, J.F., Shay, M.A., Rogers, B.N., Denton, R.E., Hesse, M., Kuznetsova, M., Ma, Z.W., Bhattacharjee, A., Otto, A., Pritchet, P.L. Geospace Environmental Modeling (GEM) Magnetic Reconnection Challenge, J. Geophys. Res., 106(A3), 3715–3719, 2001. 2.

Boer, G.J., and 13 colleagues, 1991. An intercomparison of the climates simulated by 14 atmospheric general circulation models. CAS/JSC Working Group on Numerical Experimentation, WCRP-58, 425.

Boesswetter, A., Bagdonat, T., Motschmann, U., Sauer, K., 2004. Plasma boundaries at Mars: A 3-D simulation study. Ann. Geophys. 22, 4363–4379.

Boesswetter, A., and 10 colleagues, 2007. Comparison of plasma data from ASPERA-3/Mars-Express with a 3-D hybrid simulation. Ann. Geophys. 25, 1851–1864.

Boesswetter, A., and 10 colleagues, 2009. Rosetta swing-by at Mars—An analysis of the ROMAP measurements in comparison with results of 3D multi-ion hybrid simulations and MEX/ASPERA-3 data, Ann. Geophys. 27, 2383–2398.

Bougher, S.W., Engel, S., Roble, R.G., Foster, B., 1999a. Comparative terrestrial planet thermospheres 2. Solar cycle variation of global structure and winds at equinox. J. Geophys. Res. 104 (13), 16591–16611.

Bougher, S.W., Keating, G., Zurek, R., Murphy, J., Haberle, R., Hollingsworth, J., Clancy, R.T., 1999b. Mars Global Surveyor aerobraking: Atmospheric trends and model interpretation. Adv. Space Res. 23, 1887–1897.

Bougher, S.W., Engel, S., Roble, R.G., Foster, B., 2000. Comparative terrestrial planet thermospheres 3. Solar cycle variation of global structure and winds at solstices. J. Geophys. Res. 105 (14), 17669–17692.

Bougher, S.W., Engel, S., Hinson, D.P., Forbes, J.M., 2001. Mars Global Surveyor radio science electron density profiles: Neutral atmosphere implications. Geophys. Res. Lett. 28, 3091–3094.

Bougher, S.W., Engel, S., Hinson, D.P., Murphy, J.R., 2004. MGS radio science electron density profiles: Interannual variability and implications for the martian neutral atmosphere. J. Geophys. Res. 109, E03010. doi:10.1029/2003JE002154.

Bougher, S.W., Bell, J., Murphy, J.R., Withers, P.G., López-Valverde, M., 2006. Polar warming in the Mars lower thermosphere: Seasonal variations owing to changing insolation and dust distributions. Geophys. Res. Lett. 33, L02203. doi:10.1029/2005GL024059.

Bougher, S.W., Blelly, P.-L., Combi, M., Fox, J.L., Mueller-Wodarg, I., Ridley, A., Roble, R.G., 2008. Neutral upper atmosphere and ionosphere modeling. Space Sci. Rev. 139, 107–141. doi:10.1007/s11214-008-9401-9.

Brain, D.A., 2006. Mars Global Surveyor measurements of the martian solar wind interaction. Space Sci. Rev. 126 (January), 77–112. doi:10.1007/s11214-006-9122-x.

Brain, D.A., Bagenal, F., Acuña, M.H., Connerney, J.E.P., 2003. Martian magnetic morphology: Contributions from the solar wind and crust. J. Geophys. Res. 108 (A12), 1424. doi:10.1029/2002JA009482.

Brain, D.A., Halekas, J.S., Lillis, R.J., Mitchell, D.L., Lin, R.P., Crider, D.H., 2005. Variability of the altitude of the martian sheath. Geophys. Res. Lett. 32 (18), L18203. doi:10.1029/2005GL023126.

Brecht, S.H., 1990. Magnetic asymmetry of unmagnetized planets. Geophys. Res. Lett. 17, 1243.

Brecht, S.H., 1997. Hybrid simulations of the magnetic topology of Mars. J. Geophys. Res. 102 (A3), 4743–4750.

Brecht, S.H., 2009. The loss of water from Mars: Numerical results and challenges. Icarus 206 (1), 164–173.

Brecht, S.H., Ferrante, J.R., 1991. Global hybrid simulation of unmagnetized planets: Comaprison of Venus and Mars. J. Geophys. Res. 96 (A7), 11209–11220.

Brecht, S.H., Ledvina, S.A., 2006. The solar wind interaction with the martian ionosphere/atmosphere. Space Sci. Rev. 126 (1–4), 15–38. doi:10.1007/s11214-006-9084-z.

Brecht, S.H., Thomas, V.A., 1988. Multidimensional simulations using hybrid particle codes. Comput. Phys. Comm. 48, 135–143.

Brecht, S.H., Ferrante, J.R., Luhmann, J.G., 1993. Three-dimensional simulations of the solar wind interaction with Mars. J. Geophys. Res. 98 (A2), 1345–1357.

Breus, T.K., Ness, N.F., Kryrmskii, A.M., Crider, D.H., Acuna, M.H., Connerney, J.E.P., Hinson, D., Barashyan, K.K., 2005. The effects of crustal magnetic fields and the pressure balance in the high latitude ionosphere/atmosphere at Mars. Adv. Space Res. 36 (January), 2043–2048. doi:10.1016/j.asr.2005.01.100.

Carlsson, E., and 46 colleagues, 2006. Mass composition of the escaping plasma at Mars. Icarus 182(2), 320–328. doi:10.1016/j.icarus.2005.09.020.

Chaufray, J.-Y., Modolo, R., Leblanc, F., Chanteur, G., Johnson, R.E., Luhmann, J.G., 2007. Mars solar wind interaction: Formation of the martian corona and atmospheric loss to space. J. Geophys. Res. 112 (September), E09009. doi:10.1029/2007JE002915.

Cravens, T.E., Hoppe, A., Ledvina, S.A., McKenna-Lawlor, S., 2002. Pickup ions near Mars associated with escaping oxygen atoms. J. Geophys. Res. 107 (A8). doi:10.1029/2001JA000125.

Crider, D.H., and 12 colleagues, 2002. Observations of the latitude dependence of the location of the martian magnetic pileup boundary. Geophys. Res. Lett. 29(11).

Crider, D.H., Vignes, D., Krymskii, A.M., Breus, T.K., Ness, N.F., Mitchell, D.L., Slavin, J.A., Acuña, M., 2003. A proxy for determining solar wind pressure at Mars using Mars Global Surveyor data. J. Geophys. Res. 108 (A12), 1–21. doi:10.1029/2003JA009875.

Dryer, M., Heckmann, G.R., 1967. Application of the hypersonic analog to the standing shock of Mars. Solar Phys. 2 (July), 112–124. doi:10.1007/BF00155897.

Dubinin, E., Fraenz, M., Woch, J., Roussos, E., Barabash, S., Lundin, R., Winningham, J.D., Frahm, R.A., Acuna, M., 2006. Plasma morphology at Mars. Aspera-3 observations. Space Sci. Rev. 126, 209–238. doi:10.1007/s11214-006-9039-4.

Dubinin, E., and 10 colleagues, 2008. Structure and dynamics of the solar wind/ionosphere interface on Mars: MEX-ASPERA-3 and MEX-MARSIS observations. Geophys. Res. Lett. 35.

Edberg, N.J.T., Lester, M., Cowley, S.W.H., Eriksson, A.I., 2008. Statistical analysis of the location of the martian magnetic pileup boundary bow shock the influence of crustal magnetic fields. J. Geophys. Res. 113 (August), A08206. doi:10.1029/2008JA013096.

Fang, X., Liemohn, M.W., Nagy, A.F., Ma, Y.-J., De Zeeuw, D.L., Kozyra, J.U., Zurbuchen, T.H., 2008. Pickup oxygen ion velocity space and spatial distribution around Mars. J. Geophys. Res. 113 (A2), A02210. doi:10.1029/2007j.icarus.2009.01.012.

Fang, X., Liemohn, M.W., Nagy, A.F., Luhmann, J.G., Ma, Y.-J., in press. On the effect of the martian crustal magnetic field on atmospheric erosion. Icarus, 206(1), 130–138.

Fedorov, A.and 49 colleagues, 2008. Comparative analysis of the Venus and Mars magnetotails. Planet. Space Sci. 56. doi:10.1016/j.pss.2007.12.012.

Gunnell, H., Holmstrom, M., Kallio, E., Janhunen, P., Dennerl, K., 2005. X rays from solar wind charge exchange at Mars: A comparison of simulations and observations. Geophys. Res. Lett. 31, L22801. doi:10.1029/2004GL020953.

Gunnell, H., Holmstrom, M., Barabash, S., Kallio, E., Janhunen, P., Nagy, A.F., Ma, Y., 2006. Planetary ENA imaging: Effects of different interaction models for Mars. Planet. Space Sci. 54 (2), 117–131.

Gurnett, D.A., and 10 colleagues, 2005. Radar soundings of the ionosphere of Mars. Science 310(5756), 1929–1933. doi:10.1126/science.1121868.

Haberle, R.M., Joshi, M.M., Murphy, J.R., Barnes, J.R., Schofield, J.T., Wilson, G., Lopez-Valverde, M., Hollingsworth, J.L., Bridger, A.F.C., Schaeffer, J., 1999. General circulation model simulations of the Mars Pathfinder atmospheric structure investigation/meteorology data. J. Geophys. Res. 104, 8957–8974.

Harned, D.S., 1982. Quasineutral hybrid simulation of macroscopic plasma phenomena. J. Comput. Phys. 47, 452–462.

Harnett, E.M., Winglee, R.M., 2003. The influence of a mini-magnetopause on the magnetic pileup boundary at Mars. Geophys. Res. Lett. 30 (20). doi:10.1029/2003GL017852.

Harnett, E.M., Winglee, R.M., 2006. Three-dimensional multi-fluid simulations of ionospheric loss at Mars from nominal solar wind conditions to magnetic cloud events. J. Geophys. Res. 111 (A9), A09213. doi:10.1029/2006JA011724.

Harnett, E.M., Winglee, R.M., 2007. High resolution multi-fluid simulations of the plasma environment near the martian magnetic anomalies. J. Geophys. Res. 112. doi:10.1029/2006JA012001.

Kallio, E., Janhunen, P., 2001. Atmospheric effects of proton precipitation in the martian atmosphere and its connection to the Mars–solar wind interaction. J. Geophys. Res. 106, 5617–5634.

Kallio, E., Janhunen, P., 2002. Ion escape from Mars in a quasineutral hybrid model. J. Geophys. Res. 107 (A3).

Kallio, E., Janhunen, P., 2003. Modelling the solar wind interaction with Mercury by a quasi-neutral hybrid model. Ann. Geophys. 21, 2133–2145.

Kallio, E.and 46 colleagues, 2006. Ion escape at Mars. Icarus 182, 350–359. doi:10.1016/j.icarus.2005.09.018.

Kallio, E., Fedorov, A., Budnik, E., Barabash, S., Jarvinen, R., Janhunen, P., 2008. On the properties of $O^+$ and $O_2^+$ ions in a hybrid model and in Mars Express IMA/ASPERA-3 data: A case study. Planet. Space Sci. 56, 1204–1213. doi:10.1016/j.pss.2008.03.007.

Kallio, E., Liu, K., Jarvinen, R., Pohjola, V., Janhunen, P., 2009. Oxygen ion escape at Mars in a hybrid model: High energy and low energy ions. Icarus 206 (1), 152–163.

Koutroumpa, D., Lallement, R., Modolo, R., Chanteur, G., Kharchenko, V., 2006. Charge-Exchange Induced X-rays in the martian Exosphere. 2007 AAS/AAPT Joint Meeting, American Astronomical Society Meeting 209, #35.05. Bulletin of the American Astronomical Society, vol. 38, p. 953.

Krymskii, A.M., Breus, T.K., Ness, N.F., Acuña, M.H., Connerney, J.E.P., Crider, D.H., Mitchell, D.L., Bauer, S.J., 2002. Structure of the magnetic field fluxes connected with crustal magnetization and topside ionosphere at Mars. J. Geophys. Res. 107 (A9), 1245. doi:10.1029/2001JA000239.

Ledvina, S.A., Brecht, S.H., submitted for publication. A basic martian ionospheric model: Assumption, properties and 3D hybrid implementation strategy. Icarus.

Ledvina, S.A., Ma, Y.-J., Kallio, E., 2008. Modeling and simulating flowing plasmas and related phenomena. Space Sci. Rev., 143–189. doi:10.1007/s11214-008-9384-6.

Liemohn, M.W., Ma, Y.-J., Frahm, R.A., Fang, X., Kozyra, J.U., Nagy, A.F., Winningham, J.D., Sharber, J.R., Barabash, S., Lundin, R., 2006. Mars global MHD predictions of magnetic connectivity between the dayside ionosphere and the magnetospheric flanks. Space Sci. Rev. 126 (1–4), 63–76. doi:10.1007/s11214-006-9116-8.

Liemohn, M.W., Ma, Y.-J., Nagy, A.F., Kozyra, J.U., Winningham, J.D., Frahm, R.A., Sharber, J.R., Barabash, S., Lundin, R., 2007. Numerical modeling of the magnetic topology near Mars auroral observations. Geophys. Res. Lett. 34 (24), L24202. doi:10.1029/2007GL031806.

Lillis, R.J., Engel, J.H., Mitchell, D.L., Brain, D.A., Lin, R.P., Bougher, S.W., Acuña, M.H., 2005. Probing upper thermospheric neutral densities at Mars using electron reflectometry. Geophys. Res. Lett. 32 (23), L23204. doi:10.1029/2005GL024337.

Luhmann, J.G., Acuña, M.H., Purucker, M., Russell, C.T., Lyon, J.G., 2002. The martian magnetosheath: How Venus-like? Planet. Space Sci. 50, 489–502.

Lundin, R., Zakharov, A., Pellinen, R., Barabasj, S.W.H., Borg, H., Dubinin, E.M., Hultqvist, B., Koskinen, H., Liede, I., Pissarenko, N., 1990. ASPERA/Phobos measurements of the ion outflow from the martian ionosphere. Geophys. Res. Lett. 17 (6), 873–876.

Lundin, R., Barabash, S., Holmstrom, M., Nilsson, H., Yamauchi, M., Fraenz, M., Dubinin, E.M., 2008. A comet-like escape of ionospheric plasma from Mars. Geophys. Res. Lett. 35, L18203. doi:10.1029/2008GL034811.

Ma, Y.-J., Nagy, A.F., 2007. Ion escape fluxes from Mars. Geophys. Res. Lett. 34 (8), L08201. doi:10.1029/2006GL029208.

Ma, Y., Nagy, A.F., Hansen, K.C., DeZeeuw, D.L., Gombosi, T.I., 2002. Three-dimensional multispecies MHD studies of the solar wind interaction with Mars in the presence of crustal fields. J. Geophys. Res. 107 (A10). doi:10.1029/2002JA009293.

Ma, Y., Nagy, A.F., Sokolov, I.V., Hansen, K.C., 2004. Three-dimensional multispecies high spatial resolution MHD studies of the solar wind interaction with Mars. J. Geophys. Res. 109 (July), 1837–1846. doi:10.1029/2003JA010367.

Matthews, A., 1994. Current advance method and cyclic leapfrog for 2D multispecies hybrid plasma simulations. J. Comput. Phys. 112, 102–116.

McDunn, T.L., Bougher, S.W., Murphy, J., Smith, M.D., Forget, F., Bertaux, J.-L., Montmessin, F., 2009. Simulating the density and thermal structure of the middle atmosphere (~80–130 km) of Mars using the MGCM–MTGCM: A comparison with MEX-SPICAM observations. Icarus, 206(1), 5–17.

Mitchell, D.L., Lin, R.P., Mazelle, C., Rème, H., Cloutier, P.A., Connerney, J.E.P., Acuña, M.H., Ness, N.F., 2001. Probing Mars' crustal magnetic field and ionosphere with the MGS electron reflectometer. J. Geophys. Res. 106 (E10), 23419–23427.

Modolo, R., Chanteur, G., 2008. A global hybrid model for Titan's interaction with kronian plasma: Application to the Cassini Ta flyby. J. Geophys. Res. 113, A01317. doi:10.1029/2006GL029208.

Modolo, R., Chanteur, G., Dubinin, E., Matthews, A., 2005. Influence of the solar EUV flux on the martian plasma environment. Ann. Geophys. 23, 433–444.

Modolo, R., Chanteur, G.M., Dubinin, E., Matthews, A.P., 2006. Simulated solar wind plasma interaction with the Martian exosphere: Influence of the solar EUV flux on the bow shock and the magnetic pile-up boundary. Ann. Geophys. 24 (December), 3403–3410.

Nagy, A.F., and 14 colleagues, 2004. The plasma environment of Mars. Space Sci. Rev. 111(1), 33–114. doi:10.1023/B:SPAC.0000032718.47512.9.

Pinty, B., and 13 colleagues, 2001. Radiation transfer model intercomparison (rami) exercise. J. Geophys. Res. 106, 11937–11956.

Powell, K.G., Roe, P.L., Linde, T.J., Gombosi, T.I., De Zeeuw, D.L., 1999. A solution-adaptive upwind scheme for ideal magnetohydrodynamics. J. Comp. Phys. 153, 284–309.

Russell, C.T., Chou, E., Luhmann, J.G., Gazis, P., Brace, L.H., Hoegy, W.R., 1988. Solar and interplanetary control of the location of the Venus bow shock. J. Geophys. Res. 93 (A6), 5461–5469.

Simon, S., Boesswetter, A., Bagdonat, T., Motschmann, U., 2007. Physics of the ion composition boundary: A comparative 3-D hybrid simulation study of Mars and Titan. Ann. Geophys. 25 (1), 99–115.

Slavin, J.A., Holzer, R.E., 1981. Solar wind flow about the terrestrial planets I: Modeling bow shock position and shape. J. Geophys. Res. 86 (A13), 11401–11418.

Slavin, J.A., Holzer, R.E., 1983. Solar wind flow about the terrestrial planets 2 comparison with gas dynamic theory and implications for solar–planetary interactions. J. Geophys. Res. 88 (A1), 19–35.

Spreiter, J., Summers, A., Alksne, A., 1966. Hydromagnetic flow around the magnetosphere. Planet. Space Sci., 223–253.

Spreiter, J., Summers, A., Rizzi, A., 1970. Solar wind flow past nonmagnetic planets – Venus and Mars. Planet. Space Sci. (January).

Terada, N., Kulikov, Y.N., Lammer, H., Lichtenegger, H.I.M., Tanaka, T., Shinagawa, H., Zhang, T.-L., 2009a. Atmosphere and water loss from early Mars under extreme solar wind and extreme ultraviolet conditions. Astrobiology 9 (1), 55–70. doi:10.1089/ast.2008.0250.

Terada, N., Shinagawa, H., Tanaka, T., Murawski, K., Kaneda, K., 2009b. A three-dimensional, multi-species, comprehensive MHD model of the solar wind interaction with the planet Venus. J. Geophys. Res. in press. doi:10.1029/2008JA013937.

Tóth, G., and 19 colleagues, 2005. Space weather modeling framework: A new tool for the space science community. J. Geophys. Res. 11.

Trotignon, J.G., Mazelle, C., Bertucci, C., Acuña, M.H., 2006. Martian shock and magnetic pile-up boundary positions and shapes determined from the Phobos 2 and Mars Global Surveyor data sets. Planet. Space Sci. 54 (February), 357–369. doi:10.1016/j.pss.2006.01.00.

Verigin, M.I., and 15 colleagues, 1991. Ions of planetary origin in the martian magnetosphere (PHOBOS 2/TAUS experiment). Planet. Space Sci. 39(1–2), 131–137.

Vignes, D., Acuña, M.H., Connerney, J.E.P., Crider, D.H., Rème, H., Mazelle, C., 2002. Factors controlling the location of the bow shock at Mars. Geophys. Res. Lett. 29 (9), 1–42. doi:10.1029/2001GL01451.

Withers, P., Mendillo, M., Rishbeth, H., Hinson, D.P., Arkani-Hamed, J., 2005. Ionospheric characteristics above martian crustal magnetic anomalies. Geophys. Res. Lett. 32, L16204. doi:10.1029/2005GL023483.

Zhang, T.-L., Luhmann, J.G., Russell, C.T., 1991. The magnetic barrier at Venus. J. Geophys. Res. 96 (A7), 11145–11153.